A PROCESS TO VERIFY NUMERICAL MODELS FOR SEISMIC FLUID-STRUCTURE INTERACTION IN ADVANCED REACTOR VESSELS

Ching-Ching Yu[*1], Andrew S. Whittaker[2]

[*]Corresponding author

[1]Postdoctoral Associate, Department of Civil, Structural, and Environmental Engineering, University at Buffalo, Buffalo, NY 14260, USA (cyu23@buffalo.edu)

[2]SUNY Distinguished Professor, Department of Civil, Structural, and Environmental Engineering, University at Buffalo, Buffalo, NY 14260, USA (awhittak@buffalo.edu)

ABSTRACT

Seismic design and qualification of a liquid-filled advanced nuclear reactor will have to account for fluid-structure interaction (FSI). Interaction between the tank, internal components, and contained liquid will rely on analysis of numerical models that must be verified and validated. This study demonstrates a verification process for models of a base-supported cylindrical tank by comparing numerical predictions and analytical solutions. The numerical models are consistent with the assumptions made to derive analytical solutions, namely, either a rigid or a linear elastic tank, ideal fluid, and small-amplitude, unidirectional, horizontal inputs. One software platform is used to illustrate the process. Seismic FSI analysis is performed using the Arbitrary Lagrangian-Eulerian (ALE) and Incompressible Computational Fluid Dynamics (ICFD) solvers in LS-DYNA. Reported responses are those used for design, including hydrodynamic pressures on the tank wall, shear forces and moments at the tank base, and wave heights of the contained liquid. The accuracy of the numerical results is discussed. The numerical models are verified for calculating the pressures on the tank wall and reactions at its base. Accurate simulation of wave action is challenging for both solvers. Recommendations for modeling, code development, and steps for verification are provided. Although focused on reactor vessels and one software platform, the verification process described herein is broadly applicable to liquid-filled vessels and other finite element codes.

1. INTRODUCTION

Liquid-filled cylindrical vessels (tanks) are widely used in industry, including liquefied natural gas tanks, water storage tanks, boilers in fossil power plants, and reactor vessels in nuclear power plants. Fluid-structure interaction (FSI) in these tanks, generated by earthquake shaking, must be addressed for design, equipment qualification, and risk assessment. Seismic FSI analysis of liquid-cooled advanced reactor is the focus of this paper. Figure 1 presents an example: a prototype fast reactor (PFR) filled with liquid sodium. The reactor includes a cylindrical vessel (tank) and internal components immersed or submerged in the contained liquid. Physical testing of the reactor vessel and its submerged components for seismic qualification is not feasible because of the involved large scales. Analytical solutions for calculating fluid-structure responses cannot be used because the boundary conditions, geometry, and seismic inputs do not conform with the underlying assumptions. If a reactor vessel is subjected to intense earthquake shaking, the responses of the liquid will be nonlinear, including sloshing and disengagement from the inner surfaces of the vessel, none of which can be calculated analytically. Numerical models can address these nonlinear responses using fluid-mechanics solvers, including adaptive meshing routines or defining fluid in a control volume (fluid domain) without discretizing the fluid. Examples of fluid-mechanics solvers are: the Fluent and CFX in ANSYS (ANSYS Inc., 2005), the Computational Fluid Dynamics (CFD) and Coupled Eulerian and Lagrangian (CEL) in ABAQUS (Dassault Systèmes, 2018), the Arbitrary Lagrangian-Eulerian (ALE), Incompressible Computational Fluid Dynamics (ICFD), and Smoothed Particle Hydrodynamics (SPH) in LS-DYNA (Livermore Software Technology Corporation (LSTC), 2018), and the particle finite element method (PFEM) in OpenSeesPy (Zhu et al., 2018), which is an extension of OpenSees (Mazzoni et al., 2009).

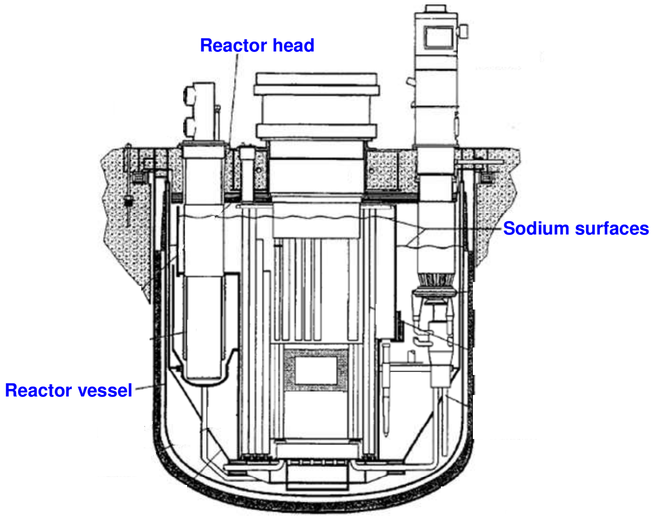

Figure 1. Prototype fast reactor (PFR), Dounreay, Scotland, constructed using stainless steel and filled with liquid sodium; dimensions of the vessel: $R = 6.1$ m, $H_s = 15.2$ m, $H \approx 0.9 H_s = 13.7$ m, and $h = 12.7$ mm (International Atomic Energy Agency (IAEA), 1999; Jensen and Ølgaard, 1995)

Numerical models used for design and qualification of safety-related nuclear equipment, such as reactors, must be *verified* and *validated*. Oberkampf and his co-workers (Oberkampf and Trucano, 2002; Oberkampf and Roy, 2010; American Institute of Aeronautics and Astronautics (AIAA), 1998) and American Society of Mechanical Engineers (ASME) (2020, 2009) provide guidance for verification and validation (V&V) of numerical models. The V&V activities depend on the application of the numerical analysis, and so the process is not unique. The guidance suggests quantifying the accuracy of a model by comparing numerical results with benchmarks: 1) *highly accurate solutions* for verification, and 2) experimental data for validation. The *highly accurate solutions* are either closed form or based on solutions to differential equations (AIAA 1998).

A majority of V&V studies were developed for solid-mechanics simulations (Oberkampf and Trucano, 2008). Although guidance for V&V of fluid-dynamics simulations is available (e.g., Oberkampf and Trucano (2002), AIAA (1998), and ASME (2009)), none is specific to models used for seismic analysis of liquid-filled reactor vessels, which is the focus of this paper.

As presented in Figure 1, a liquid-cooled advanced reactor is composed of a cylindrical tank, liquid, and immersed (or submerged) components. Per Oberkampf and Trucano (2008), the benchmarks (i.e., analytical solutions and experimental results) used for V&V here are developed based on a hierarchy of complexity in the geometry and liquid (fluid) responses in the reactor vessel. The reactor is parsed into a liquid-filled cylindrical tank and immersed (or submerged) components. Table 1 presents companion studies (Yu and Whittaker, 2021a; Yu et al., 2021; Mir et al., 2020) to those described in this paper.

Table 1. Studies in the verification and validation for seismic FSI models of a liquid-cooled advanced reactor, parsed into a cylindrical tank and internal components

	Verification	Validation
Cylindrical tank	Presented here	Yu et al. (2021); Mir et al. (2020)
Cylindrical tank and internal components	Yu and Whittaker (2021a)	Mir et al. (2021)

A number of studies have addressed verification of FSI models for liquid-filled tanks, but none, to the knowledge of the authors, have considered all fluid-structure responses critical to the seismic design of reactor vessels (e.g., pressures, reactions at supports, and wave heights). Ma et al. (1983) and Fujita et al. (1984) both developed numerical formulations for seismic FSI analysis of reactor vessels. Ma et al. (1983) compared numerical and analytical results for fundamental frequencies of wave actions in a vessel, and Fujita et al. (1984) compared those for wave heights. Christovasilis and Whittaker (2008) and Goudarzi and Sabbagh-Yazdi (2012) used ANSYS for seismic FSI analysis of cylindrical and rectangular tanks, respectively. Christovasilis and Whittaker (2008) compared numerical results for wave heights and reactions at the base of a cylindrical tank with those calculated using a mechanical analog derived from analytical solutions. Goudarzi and Sabbagh-Yazdi (2012) verified numerical models for wave heights in six rectangular tanks with different dimensions.

The verification process presented here aligns most closely with that provided in AIAA (1998), and considers critical fluid-structure responses in reactor vessels. Analytical solutions derived by Veletsos (1984), Jacobsen (1949), and Yu and Whittaker (2020, 2021b) are used as benchmarks. The ALE and ICFD solvers in LS-DYNA (2018), which are widely used in earthquake engineering and nuclear industry, are used here for numerical analysis of a rigid and an elastic (flexible) tank. Although this paper focuses on reactor vessels and one software platform, the verification process described herein is broadly applicable to liquid-filled vessels and other software packages.

Section 2 defines the process of verification. Section 3 introduces the benchmark, which are the analytical solutions used in the verification exercise. Section 4 describes numerical models for cylindrical tanks. Section 5 presents input motions used for seismic FSI analysis of the tanks. Section 6 verifies the models by comparing the numerical and analytical results for fluid-structure responses. Section 7 presents a summary and conclusions of the verification exercise and recommended steps for the process.

2. IMPLEMENTATION OF A VERIFICATION PROCESS

The process of verification defined in AIAA (1998) is implemented here: quantifying the accuracy of a numerical model by comparing analysis results with *correct answers*. Figure 2a presents the AIAA process, involving a *conceptual model*, *computational model*, *computational solution*, and *correct answer provided by highly accurate solutions*. The computational model, termed a numerical model in this paper, is the subject of verification. The computational solution is the numerical result of a response quantity important to the analysis. This numerical model is constructed based on a conceptual model relevant to the application of the numerical analysis. The conceptual model has physical properties (e.g., geometry, boundary conditions, initial conditions, and mechanical properties) for which accurate solutions are available. A correct answer is generated using highly accurate solutions: analytical solution (closed-form solution), ODE, or PDE, as noted in Figure 2a. Accordingly, the physical properties used for the conceptual model, computational model, and the highly accurate solutions are identical. The computational model is verified by comparing the computational solution for and correct answer to the response quantity.

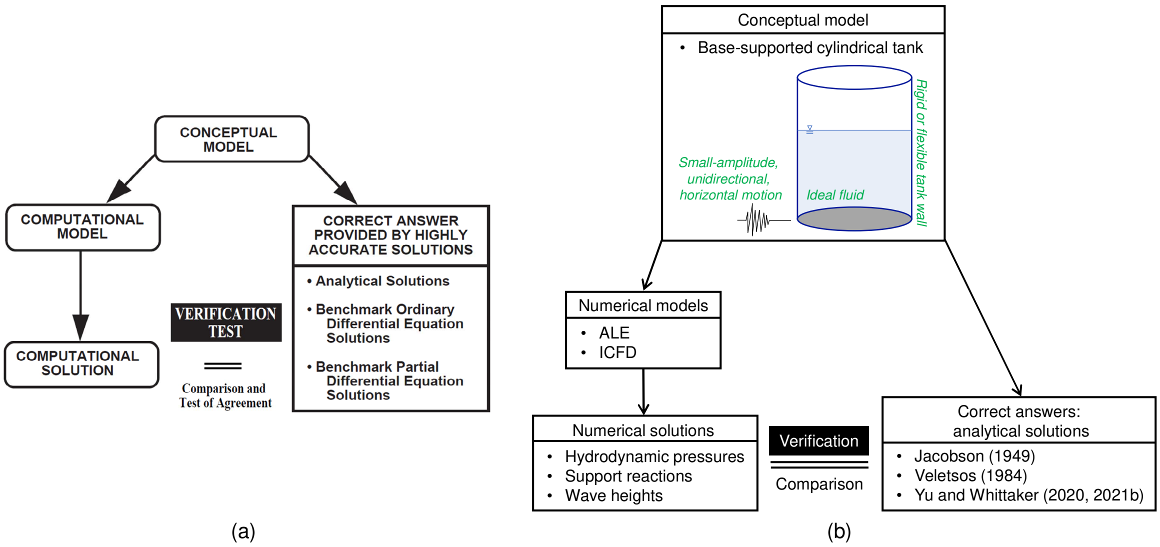

Figure 2. Verification process: (a) defined by AIAA (1998); (b) implemented here

The studies presented in this paper implement the process of Figure 2a to verify numerical models of a liquid-cooled advanced reactor vessel: Figure 2b. The conceptual model used here is a liquid-filled tank, for which analytical solutions are available: Jacobsen (1949), Veletsos (1984), and Yu and Whittaker (2020, 2021b). The conceptual model must accommodate the geometry, boundary conditions, initial conditions, and mechanical properties of the tank assumed for the derivations of the analytical solutions. Figure 2b presents a schematic view of the conceptual model: a rigid or flexible, cylindrical, base-supported tank, filled with an ideal fluid, and subjected to small-amplitude, unidirectional, horizontal motion. The numerical models are developed for this conceptual tank and analyzed using the ALE and ICFD solvers in LS-DYNA. The numerical solutions are calculated for fluid-structure responses critical to the seismic design of the reactor vessel: hydrodynamic pressures on the tank wall, reactions (i.e., shear forces and moments) at the tank base, and wave heights of the contained liquid. Each numerical model (i.e., ALE or ICFD) is verified by comparing the results for the responses with those calculated using the analytical solutions.

AIAA (1998) noted that investigation for temporal (i.e., time step), spatial (i.e., mesh size), and iterative convergence in numerical analysis are crucial to the verification process. The numerical results (see Section 6) presented in this paper are generated using the optimized numerical models (see Section 4) developed via sensitivity analyses for the temporal and spatial discretizations and the number of computational iterations. The sensitivity analyses and convergence are not within the scope of this paper and so are not discussed.

3. ANALYTICAL SOLUTIONS: AN INTRODUCTION

Jacobsen (1949) and Veletsos (1984) developed analytical solutions for fluid-structure responses of liquid (fluid)-filled base-supported cylindrical tanks subjected to unidirectional horizontal motions. The fluid response was assumed to be linear, and so the analytical solutions are strictly applicable to small-amplitude motions. The fluid-structure response was parsed into an impulsive and a convective component, shown using the accelerating tank in Figures 3a and b, respectively. The impulsive response is generated by the part of the fluid accelerating with the tank horizontally. The convective response is generated by the other part of the fluid assumed not to move with the tank but to oscillate vertically and induce waves. Per Figure 3a, the fluid associated with the impulsive component is attached to the inner surfaces of the tank and generates pressures p_{imp} in the fluid and on these surfaces. The resultant force of p_{imp} on the tank wall (orange arrows) is balanced by a shear force in the x direction, F_{imp}. The resultant moments of p_{imp} on the wall (orange arrows) and base (pink arrows) are balanced by moments at the tank base about the y axis, $M_{imp,w}$ and $M_{imp,b}$, respectively. Per Figure 3b, the fluid associated with the convective component generates waves: the free surface oscillates vertically by a small displacement d_w (termed wave height hereafter), at a convective frequency f_{con}. The wave action induces convective pressures p_{con} in the fluid and on the inner surfaces of the tank, which are balanced by reactions at the tank base F_{con}, $M_{con,w}$, and $M_{con,b}$ (counterparts of F_{imp}, $M_{imp,w}$, and $M_{imp,b}$, respectively).

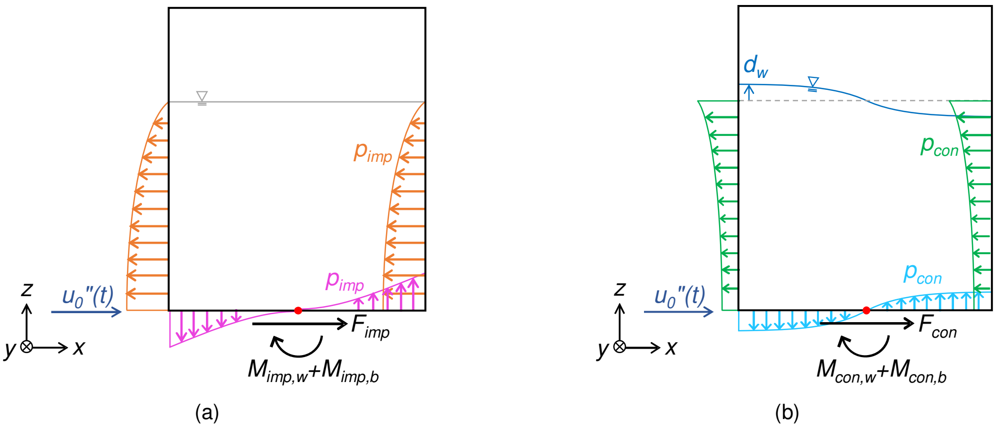

Figure 3. FSI in a vertical cross section of a base-supported tank accelerating in the x direction: (a) impulsive: pressures, p_{imp}, on the walls and base; shear force, F_{imp}, and moments, $M_{imp,w}$ and $M_{imp,b}$, at the base; (b) convective: wave height, d_w; pressures, p_{con}, on the walls and base; shear force, F_{con}, and moments, $M_{con,w}$ and $M_{con,b}$, at the base

Jacobsen (1949) assumed the tank to be rigid and derived analytical solutions for impulsive pressures, termed p_1, and resultants of p_1 at the tank base: a shear force, X_1, and two moments, M_1, and N_1. The pressure p_1 is identical to p_{imp} defined in Figure 3a, and the resultant forces are balanced by the reactions at the tank base: $F_{imp} = -X_1$, $M_{imp,w} = -M_1$, and $M_{imp,b} = -N_1$. The solutions presented in Jacobsen (1949) involve calculation errors, and were corrected and re-derived in Yu and Whittaker (2020, 2021b). Table 2 lists the equation numbers for the analytical solutions presented in Jacobsen (1949) and those corrected by Yu and Whittaker (2020, 2021b).

Veletsos considered tank flexibility and assumed the tank to be full for deriving impulsive responses. The tank was assumed to be rigid for deriving convective responses. Veletsos decoupled impulsive and convective responses into modal contributions, and derived solutions for each mode. For the impulsive component, the solutions of Veletsos addressed the impulsive frequency $f_{imp,k}$ of the k th mode, and the modal responses: $p_{imp,k}$, $F_{imp,k}$, $M_{imp,w,k}$, and $M_{imp,b,k}$ (termed P_i, Q_i, M_i, and ΔM_i, respectively, in Veletsos (1984)). For the convective component, the solutions addressed $f_{con,j}$, $p_{con,j}$, $F_{con,j}$, $M_{con,w,j}$, $M_{con,b,j}$, and $d_{w,j}$ in the j th convective mode (termed f_j, P_c, Q_c, M_c, ΔM_c, and d, respectively, in Veletsos (1984)). The sign convention was not defined clearly in Veletsos (1984), and minus signs in some solutions were ignored or omitted. These solutions were re-worked in Yu and Whittaker (2020, 2021b). Tables 3 and 4 list the equation numbers and references (Yu and Whittaker, 2020, 2021b; Veletsos, 1984) for the analytical solutions of the impulsive and convective responses, respectively.

Table 2 Equation numbers of analytical solutions for impulsive responses presented in Jacobsen (1949) and those corrected in Yu and Whittaker (2020, 2021b), rigid, base-supported, cylindrical tanks, unidirectional horizontal motion of a small amplitude

	p_{imp}	F_{imp}	$M_{imp,w}$	$M_{imp,b}$
Jacobsen (1949)	16	17	--[a]	19
Yu and Whittaker (2020, 2021b)	3.9, 1	3.11, 4	3.12, 6	3.13, 8

a. No equation number was assigned to $M_{imp,w}$ in Jacobsen (1949). The analytical solution was presented between Eqs. (18) and (19).

Table 3. Equation numbers of analytical solutions for impulsive frequencies and responses presented in Veletsos (1984) and those re-worked in Yu and Whittaker (2020, 2021b), flexible, base-supported, cylindrical tanks, unidirectional horizontal motion of a small amplitude

	$f_{imp,k}$	$p_{imp,k}$	$F_{imp,k}$	$M_{imp,w,k}$	$M_{imp,b,k}$
Veletsos (1984)[a]	7-52	7-44	7-45	7-46	7-47
Yu and Whittaker (2020, 2021b)	3.52, 11	3.59, 12	3.61, 13	3.62, 14	3.63, 15

a. The sign convention was not defined clearly. See Yu and Whittaker (2020, 2021b) for more information.

Table 4. Equation numbers of analytical solutions for convective frequencies and responses presented in Veletsos (1984) and those re-worked in Yu and Whittaker (2020, 2021b), rigid, base-supported, cylindrical tanks, unidirectional horizontal motion of a small amplitude

	$f_{con,j}$	$p_{con,j}$	$F_{con,j}$	$M_{con,w,j}$	$M_{con,b,j}$	$d_{w,j}$
Veletsos (1984)[a]	7-8 C-27	7-3 C-45	7-16[b] C-30	7-21[b] C-32	7-22[b] C-34	7-36 C-46
Yu and Whittaker (2020, 2021b)	3.73, 18	3.79, 21	3.82, 27	3.83, 29	3.84, 31	3.81, 24

a. The sign convention was not defined clearly. See Yu and Whittaker (2020, 2021b) for more information.
b. The impulsive and convective components were algebraically summed. See the second term of the equations for the convective component.

All analytical solutions listed in Tables 2, 3, and 4 are functions of the tank radius R, the fluid height H, the fluid density ρ, and the x-directional seismic input $u_0''(t)$, noted in Figure 4. If tank flexibility is taken into account, the solutions (Table 3) are further functions of the wall thickness h and the mechanical properties of the tank: density ρ_s, elastic modulus E_s, and Poisson's ratio υ_s. The solutions of p_{imp} and p_{con} are functions of cylindrical coordinates (r, θ, z) shown in Figure 4, which enables the determination of pressures at any location in the fluid and on the wall and base of the tank. All responses (i.e., p_{imp}, F_{imp}, $M_{imp,w}$, $M_{imp,b}$, p_{con}, F_{con}, $M_{con,w}$, $M_{con,b}$, and d_w) are functions of time t, and so the product of each solution is a time series. More information on the analytical solutions can be found in Jacobsen (1949), Veletsos (1984), and Yu and Whittaker (2020, 2021b).

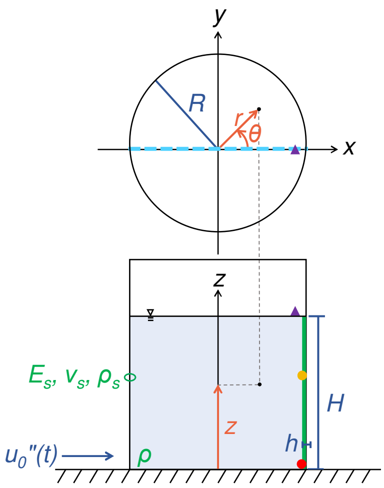

Figure 4. Variables used in the analytical solutions (Jacobsen, 1949; Veletsos, 1984; Yu and Whittaker, 2020, 2021b) shown on two cutaway views of a cylindrical tank, a Cartesian coordinate system (x, y, z), and a cylindrical coordinate system (r, θ, z); locations for reporting responses: hydrodynamic pressures at the red and yellow solid circles and along the green line, and wave heights at the purple triangle and along the blue dashed line

4. NUMERICAL MODELS

Numerical models for seismic FSI analysis are developed for the tank of Figure 2b, namely, consistent with the assumptions made to derive the analytical solutions (Jacobsen, 1949; Veletsos, 1984). The radius, R, and height, H_s, of the tank are 0.79 m and 2 m, respectively, loosely based on the geometry of a length-scaled advanced reactor vessel. Response-history analysis of the tank subjected to x-direction shaking is performed using the ALE and ICFD solvers in LS-DYNA. The ALE solver uses an explicit analysis and models fluid using Eulerian elements. These elements do not deform with fluid motions but rather serve together as a grid of integration points in the fluid domain. The ICFD solver adopts an implicit analysis to model a fluid using Lagrangian elements. These elements are generated by the solver automatically in a defined domain and are highly deformable to accommodate fluid motions. Although nonlinear fluid responses can be addressed by the solvers, only linear responses are involved in the analysis performed here to be comparable to the analytical solutions. To verify the models, numerical and analytical results of linear fluid-structure responses are compared, including hydrodynamic pressures on the tank wall, reactions (i.e., shear forces and moments) at the tank base, and wave heights.

The key cards and parameters used to build the models are identified to enable a reader to either replicate the models in LS-DYNA or help build a model in another software platform.

4.1. RIGID TANK

Two fluid heights, $H = 1.2$ and 1.8 m, are considered for the numerical models of the rigid tank. The models and results for $H = 1.8$ m are presented in this paper, and those for $H = 1.2$ m can be found in Yu and Whittaker (2020). Figures 5 and 6 present the ALE and ICFD models, respectively, and global coordinates (x, y, z) consistent with those in Figure 4. Figures 5a, b, and c present different parts of the ALE model. The tank is shown in blue, and the water is shown in yellow. A vacuum space shown in grey is built above the water. The water and vacuum in each model together define a fluid domain. The tank is modeled using Lagrangian, four-node, shell elements, and the water and vacuum are modeled using Eulerian, eight-node, solid elements. The nodes of the tank, water, and vacuum are merged on their interfaces. Air was not considered in the analytical solutions, and so is not included in the models.

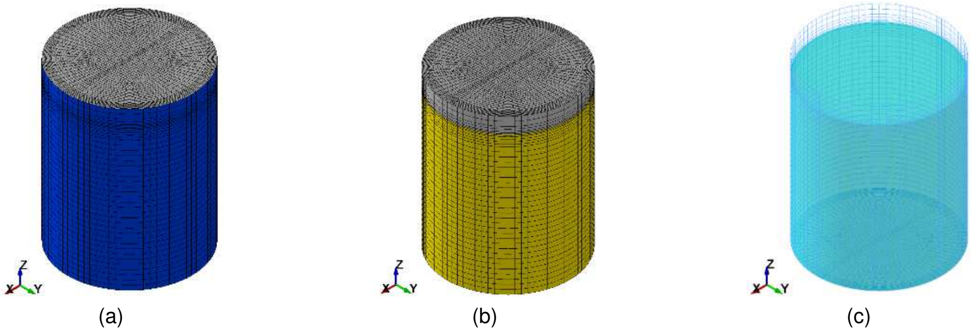

Figure 5. ALE model of a rigid cylindrical tank with $R = 0.79$ m, $H_s = 2$ m, and $H = 1.8$ m: (a) tank and vacuum; (b) water and vacuum; (c) water at $t = 0$

The sizes of the elements for the ALE model shown in Figures 5a and b are optimized, resulting in finer mesh for the fluid domain adjacent to the tank wall, around the boundary between the water and vacuum (i.e., free surface), and along the tank diameter in the direction of the seismic input (i.e., x direction). Figure 5c presents the contained water with a depth of 1.8 m, at the first step of the analysis (i.e., time $t = 0$).

Figures 6a and b present fluid elements of the ICFD model. Since the tank is rigid, namely no deformations, the presence of the tank does not affect fluid responses. The ICFD analysis for coupling of the structural (i.e., tank) and fluid elements is computationally expensive. For the purpose of efficiency, the ICFD model herein excludes the rigid tank and includes the fluid domain (i.e., water and vacuum) only. (For a flexible tank, the deformation of the tank affects fluid responses, and so the model has to include both. Information on the ICFD model of a flexible tank that addresses the coupling of structural and fluid elements is presented in Section 4.2.) The run time of this ICFD model reduces by a factor of 8, by comparison with that of a companion model including both the rigid tank and fluid. (Information of the analysis computer: 7th Gen (i7) 4-core Intel processor, 32 GB RAM, and 512 GB SSD.)

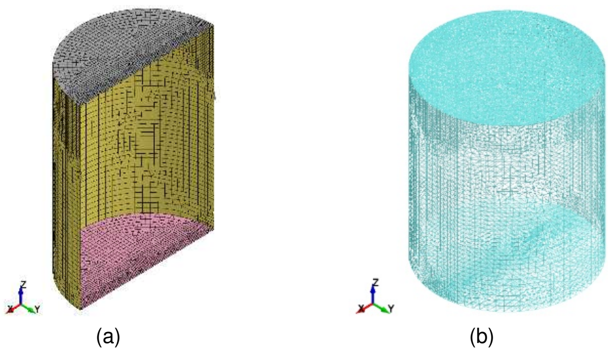

Figure 6. ICFD model of a rigid cylindrical tank with $R = 0.79$ m, $H_s = 2$ m, and $H = 1.8$ m: (a) surfaces for a half fluid domain; (b) water at $t = 0$

Figure 6a presents a half fluid domain in the ICFD model built using three surfaces: 1) adjacent to the tank base (shown in pink), 2) adjacent to the tank wall (shown in yellow), and 3) horizontally closing the top of the domain (shown in grey). The fluid surfaces are built using Lagrangian three- and/or four-node shell elements. Finer mesh for fluid surfaces results in more accurate responses but also a longer run time. The mesh shown in Figure 6a is determined by a trade-off between accuracy and run time, which is bounded by 5 days for a 12-second input motion, E-1, that is used for analysis here. (The input motion is described in Section 5.) Smaller elements are used along the diameter of the fluid domain in the direction of the seismic input: x direction. The initial height of the free surface, $H=$ 1.8 m, is defined using the *ICFD_INITIAL_LEVELSET card. The *MESH_BL card is used to generate finer water elements adjacent to the inner surfaces of the tank. The finite elements of the water enclosed by the yellow and pink surfaces in Figure 6a and the defined free surface is automatically generated by the ICFD solver at $t=0$. The water is constructed using Lagrangian four-node solid elements, as shown in Figure 6b.

A wall thickness and mechanical properties are assigned to the tank in the ALE model. (The tank is excluded from the ICFD model.) To accommodate the analytical solutions (Jacobsen, 1949), which addressed hydrodynamic loadings only, the inertial force of the tank must be negligible in the numerical calculations. Accordingly, a tiny thickness h=0.5 mm and density $\rho_s = 100$ kg/m^3 is assigned to the shell elements of the tank to reduce its mass. The elastic modulus, $E_s = 2\times10^{11}$ N/m^2, and Poisson's ratio, $\upsilon_s = 0.27$ consistent with carbon steel are used. These values do not affect the responses of the rigid tank but must be defined in the model. No damping is applied to the tank, namely, the damping ratio=0.

The contained fluid is ideal, namely, inviscid and incompressible. The density of water, $\rho = 1000$ kg/m^3, and zero viscosity, $\mu = 0$, are assigned to the yellow elements in the ALE model of Figure 5b and the pink and yellow fluid surfaces in the ICFD model of Figure 6a. The ICFD solver can accommodate only incompressible fluids, whereas the ALE solver addresses the compressibility of the fluid through the *EOS_LINEAR_POLYNOMIAL card. To achieve incompressibility, the bulk modulus K_w defined in the card (termed $C1$) for the water must be sufficiently large. A sensitivity analysis is performed for $C1 = 2.15\times10^9$ N/m^2 (i.e., the bulk modulus of water at 25°C), 5×10^9 N/m^2, and 2×10^{10} N/m^2. The differences in the results are negligible, but the run time of the analysis significantly increases with an increasing bulk modulus, and so the value consistent with water $K_w = 2.15\times10^9$ N/m^2 is used for the ALE model. The vacuum space in the ALE model, namely, the grey elements of Figure 5b, is assigned void properties through the *INITIAL_VOID card. The elements of the grey fluid surface in the ICFD model of Figure 6a are assigned a zero density and viscosity.

The mass of the contained water is 3527 kg in both the ALE and ICFD models and that of the tank in the ALE model is 0.6 kg, which is negligible by comparison with the water. The gravitational acceleration g of 9.81 m/s^2 is assigned to the z direction.

4.2. FLEXIBLE TANK

Figures 7 and 8 present ALE and ICFD models, respectively, for a flexible tank and the global coordinates (x, y, z). To accommodate the assumption used in the analytical solutions (Veletsos, 1984), the flexible tank is full (i.e., $H = 2$ m) and wave action (i.e., convective response) is not taken into account. Figures 7a, b, and c present different parts of the ALE model. The tank is shown in blue, and the water is shown in yellow. A 0.2-m deep vacuum space shown in grey is built at the top of the water and beyond the height of this full tank. With the presence of the vacuum space, a free surface is formed at the top of the water, where the pressure is zero.

The elements used here are identical to those in the ALE model for the rigid tank in Section 4.1: 1) Lagrangian, four-node, shell elements for the tank, and 2) Eulerian, eight-node, solid elements for the water and vacuum. The nodes of the tank, water, and vacuum are merged at their interfaces. The sizes of the elements shown in Figures 7a and b are similar to those used for the rigid tank presented in Figures 5a and b: finer mesh adjacent to the tank wall and along the x direction. Figure 7c presents the water in the tank at $t = 0$.

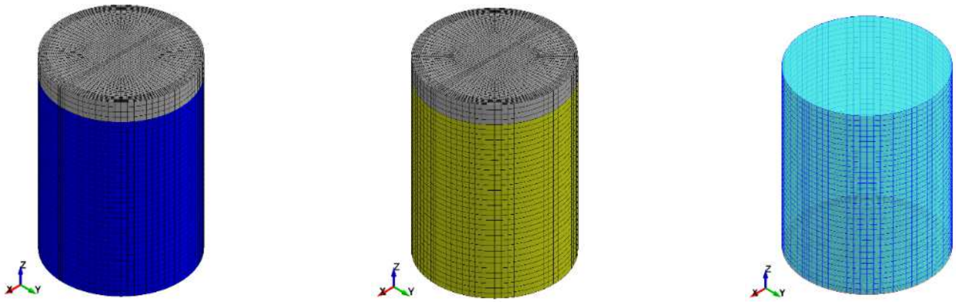

(a) (b) (c)

Figure 7. ALE model of a flexible base-supported tank with $R = 0.79$ m, $H_s = 2$ m, and $H = 2$ m: (a) tank and vacuum; (b) water and vacuum; (c) water in the tank at $t = 0$

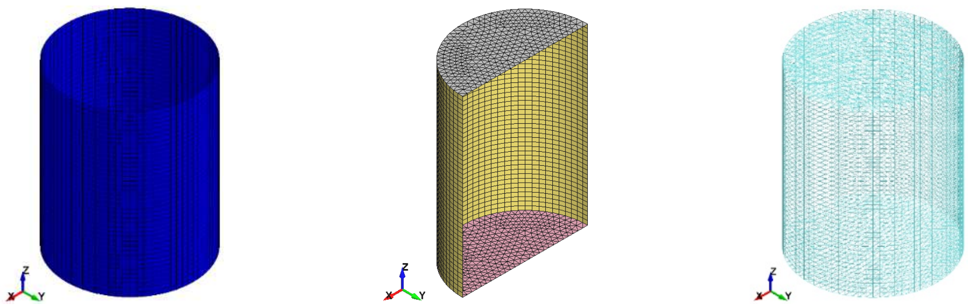

(a) (b) (c)

Figure 8. ICFD model of a flexible base-supported tank with $R = 0.79$ m, $H_s = 2$ m, and $H = 2$ m: (a) tank; (b) surfaces for a half fluid domain; (c) water at $t = 0$

Figures 8a, b, and c present different parts of the ICFD model. The tank is shown in blue in Figure 8a. Figure 8b presents a half fluid domain, built using three surfaces (yellow, pink, and grey) to define the boundaries. The tank and the fluid surfaces do not share nodes at their interfaces. The interaction between the tank and water is activated by the *ICFD_BOUNDARY_FSI card. The sizes of the fluid elements of Figure 8b are larger than those used for the rigid tank presented in Figure 6a because wave action, which requires fine meshes, is excluded from the analysis of the flexible tank here. The height of the fluid domain is 2.2 m and greater than the tank height, $H_s = 2$ m, namely a 0.2-m thick vacuum space with zero pressure is provided on the top of the water. The height of the free surface, $H = 2$ m, is defined using the *ICFD_INITIAL_LEVELSET card. The *MESH_BL is assigned to the yellow and pink surfaces in Figure 8b to generate finer water elements adjacent to the tank wall and base. Elements for the water are automatically generated by the ICFD solver at $t = 0$, as shown in Figure 8c. The elements used for the ICFD model are all Lagrangian: 1) four-node shells for the tank, 2) three- or four-node shells for the fluid surfaces, and 3) four-node solids for the water.

The analytical solutions (Veletsos, 1984) assumed the tank wall is flexible and the base is rigid. The elements of the wall and base are assigned elastic and rigid materials, respectively, with the mechanical properties consistent with carbon steel: ρ_s = 7850 kg/m^3, E_s = 2×10^{11} N/m^2, and $\upsilon_s = 0.27$. A wall thickness $h = 0.4$ mm is used here, which achieves a reasonable first impulsive frequency, $f_{imp,1}$, of the flexible tank: 24.1 Hz, estimated using Eq. (7-52) in Veletsos (1984) per Table 3. For the PFR vessel presented in Figure 1, of which the geometries are similar to the modeled flexible tank (e.g., $H_s / R \approx 2.5$), $f_{imp,1} = 6.4$ Hz per Veletsos' solution. As noted in Section 1, the length scale of the flexible tank is 1/10. If the length scale of 1/10 is used for the PFR vessel, its $f_{imp,1}$ is scaled by a factor of $\sqrt{10}$, namely, 20.3 Hz ($\sqrt{10}\times 6.4$), which is comparable to that of the flexible tank modeled here: 24.1 Hz. A target damping ratio of 2% is assigned using the *DAMPING_FREQUENCY_RANGE_DEFORM card to the elements of the tank wall for a frequency range of 15 to 250 Hz, which includes the first five impulsive modes of the filled flexible tank per Eq. (7-52) in Veletsos (1984): 24 to 135 Hz. The damping achieved by the card in the numerical simulation varies as a function of frequency between 0.1% and 4% (Huang et al., 2019). No damping is applied to the tank base since it is rigid: damping ratio=0.

The models of the water are assigned the mechanical properties identical to those for the rigid tank described in Section 4.1. The masses of the flexible tank and the contained water are 38 and 3921 kg, respectively, in both ALE and ICFD models. The mass of the tank is negligible: less than 1% of the water mass.

The analytical solutions of Veletsos (1984) for flexible tanks addressed only the impulsive component of fluid-structure responses. The convective component must be removed from numerical analysis to enable verification. Convective responses are generated by the part of the fluid oscillating vertically. The vertical oscillation changes the potential energy of the fluid, which is transformed from the kinetic energy generated by fluid velocities. The potential energy can only appear if the gravitational acceleration g exists. Accordingly, to remove the convective component from fluid-structure responses, g is not assigned to the models.

5. INPUT MOTIONS

Table 5 lists the unidirectional horizontal input motions used for the FSI analysis. Four motions are used for the rigid tank: two sinusoidal motions (S-1 and S-2) and two earthquake motions (E-1 and E-2). Three motions are used for the flexible tank: a sine-sweep motion (S-S), S-1, and E-1. Motions S-1, S-2, E-1, and E-2 are used to generate fluid-structure responses of the rigid and/or flexible tanks, and S-S is used to identify the impulsive frequencies of the flexible tank. To accommodate the assumption of linear fluid responses used for the analytical solutions, the peak ground accelerations (PGAs) for the motions listed in Table 5 are all small (i.e., 0.025 to 0.2 g). The linearity and amplitude of fluid responses depend on both 1) the dimensions and mechanical properties of the tank and fluid, and 2) the frequency content of the seismic input. Accordingly, the PGA values used for the rigid and flexible tanks and the five motions here are not identical.

Sinusoidal motions S-1 and S-2 are used to drive impulsive responses of the flexible tank and convective responses of the rigid tank, respectively. The frequency of S-1 is 20 Hz and 8 cycles are included, namely, the duration of the motion is 0.4 (=8/20) second. The frequency of 20 Hz is very close to the first impulsive frequency of the flexible tank (i.e., $f_{imp,1} = 24.1$ Hz), and so a tiny PGA=0.02 g is used to avoid nonlinear responses and instability. Motion S-2 includes 2 cycles of a 0.5-Hz sine wave, and so the duration is 4 (=2/0.5) seconds. The frequency of 0.5 Hz is selected to be sufficiently close to the first convective frequency, $f_{con,1} = 0.76$ Hz, estimated using Eq. (7-8) in Veletsos (1984) per Table 4. A frequency of the sinusoidal motion greater than 0.5

Hz and closer to $f_{con,1}$ could induce intense sloshing, which is not accommodated by the analytical solutions. A tiny PGA of 0.025 g is used for this wave-driving motion to suppress the vertical accelerations of the free surface in the numerical models since the analytical solution assume this acceleration to be zero.

Table 5. Input motions for response-history analysis of the rigid and flexible tanks

	Motions	Rigid tank (PGA)	Flexible tank (PGA)
Sinusoidal	S-1	✓ (0.2 g)	✓ (0.02 g)
	S-2	✓ (0.025 g)	--
Earthquake	E-1	✓ (0.2 g)	✓ (0.05 g)
	E-2	✓ (0.025 g)	--
Sine-sweep	S-S	--	✓ (0.2 g)

The two earthquake motions, E-1 and E-2, are records of the 1940 El Centro earthquake in California, U.S. and the 1999 Chi-Chi earthquake in Taiwan, respectively. Table 6 lists information on the two earthquake records. Consistent with the length scale of the tank, the time scale of each earthquake motion is compressed by a factor of $\sqrt{10}$. Figure 9 presents time series and 2%-damped acceleration spectra for E-1 and E-2, with the compressed time scale and PGAs of 1 g. Per Figures 9c and d, the frequency contents of the two motions are very different. Significant spectral acceleration of E-1 is in the range of 5 to 30 Hz, and that of E-2 is in the range of 1 to 4 Hz.

Table 6. Information of the earthquake records[1] used for response-history analysis

	Event	Year	Station	Direction	Original PGA
E-1	El Centro Earthquake (Imperial Valley-02)	1940	El Centro Array #9	180	0.28 g
E-2	Chi-Chi Earthquake	1999	TCU052	EW	0.36 g

1. Records are extracted from the PEER Ground Motion Database (http://ngawest2.berkeley.edu/, accessed on March 18, 2019)

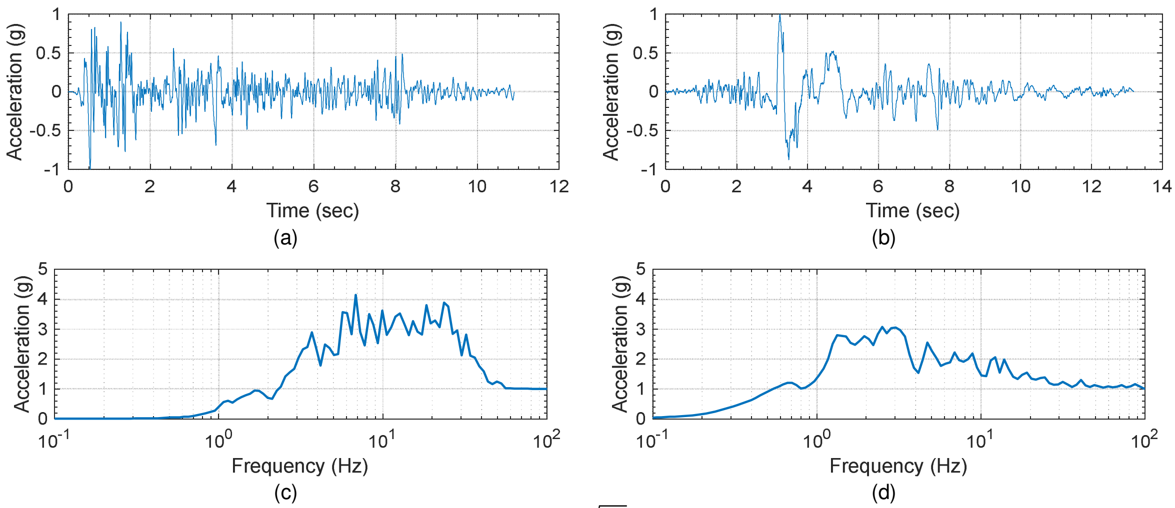

Figure 9. Earthquake records with a time scale of $1/\sqrt{10}$ and PGA of 1 g (a) time series of E-1; (b) time series of E-2; (c) 2%-damped acceleration spectrum of E-1; (d) 2%-damped acceleration spectrum of E-2

The PGAs of E-1 and E-2 are scaled (from the original values listed in Table 6) to a small amplitude. Per Table 5, the PGAs of E-1 and E-2 used for the rigid tank are 0.2 and 0.025 g, respectively. The PGA of E-2 is scaled to a tiny value (0.025 g) since its spectral acceleration at $f_{con,1}$ of 0.76 Hz is relatively high (by comparison with E-1), which could induce nonlinear wave action. For the flexible tank, E-1 is used for the analysis and the PGA is scaled to 0.05 g. A small PGA=0.05 g is used here because the spectral acceleration around $f_{imp,1}$ of 24.1 Hz is significant, which could induce nonlinear fluid responses and instability.

The impulsive frequencies of the flexible tank in the models are identified from responses to S-S since the ALE and ICFD solvers cannot perform eigenvalue analysis. The PGA of S-S is 0.2 g. The frequency band of S-S ranges between 0.25 and 150 Hz, which enables the identification of the first three impulsive frequencies between 20 and 100 Hz. Figure 10 presents the time series and Fourier amplitude spectrum of S-S.

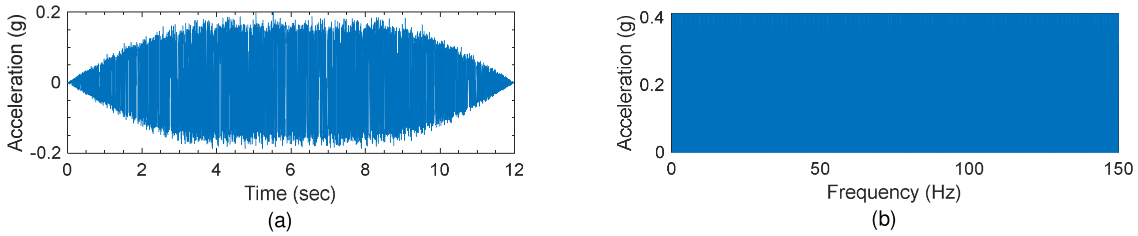

Figure 10. Sine-sweep motion S-S, unidirectional horizontal input, PGA=0.2g, frequency band of 0.25 to 150 Hz: (a) time series; (b) Fourier amplitude spectrum

6. RESULTS AND VERIFICATION

6.1. RIGID TANK

Analytical solutions are used to verify the numerical models of a rigid, base-supported, cylindrical tank ($R = 0.79$ m, $H_s = 2$ m, $H = 1.8$ m), subjected to S-1, S-2, E-1, and E-2. The equation numbers and references (Jacobsen, 1949; Veletsos, 1984; Yu and Whittaker, 2020, 2021b) of the analytical solutions for impulsive and convective responses of rigid tanks are presented in Tables 2 and 4, respectively. The corrected solutions per Yu and Whittaker (2021b) are used here. Per Table 2, the impulsive responses include p_{imp}, F_{imp}, $M_{imp,w}$, and $M_{imp,b}$. Per Table 4, the convective responses are decoupled into modal contributions. The solutions address $f_{con,j}$, $p_{con,j}$, $F_{con,j}$, $M_{con,w,j}$, $M_{con,b,j}$, and $d_{w,j}$ in the jth convective mode. Damping is set to zero for the calculation of impulsive and convective responses, to be consistent with the numerical models.

Response time series of the numerical models and analytical solutions are compared for the hydrodynamic pressure on the tank wall, p_w, the shear force at the tank base in the x direction, F, the moment at the tank base about the y axis, M_{wb}, and the wave height, d_w. Numerical results combine both impulsive and convective components, and so the analytical solutions of the two components are algebraically summed to enable the comparison. Each convective response is the infinite algebraic sum of modal responses (i.e., $j = 1$ to ∞), and ten modes are considered here since the contributions of the eleventh and higher modes are negligible. As an example, the analytical expression for p_w is as follows:

$$p_w = p_{imp} + \sum_{j=1}^{10} p_{con,j} \quad (1)$$

where the equations of p_{imp} and $p_{con,j}$ are taken from Yu and Whittaker (2021b), referenced in Tables 2 and 4. The wave height, d_w, is contributed by convective modes only (ten modes are included here), and no impulsive component is involved. The moment at the tank base, M_{wb}, calculated per numerical analysis, includes components that balance the hydrodynamic pressures on the wall and base together: M_w and M_b. Accordingly, the analytical counterpart is calculated as:

$$M_{wb} = M_w + M_b = (M_{imp,w} + \sum_{j=1}^{10} M_{con,w,j}) + (M_{imp,b} + \sum_{j=1}^{10} M_{con,b,j}) \quad (2)$$

where the equations are $M_{imp,w}$, $M_{con,w,j}$, $M_{imp,b}$, and $M_{con,b,j}$ are taken from Yu and Whittaker (2021b), referenced in Tables 2 and 4.

Response time series for E-1 and E-2 are presented in Sections 6.1.1 to 6.1.3, and those for S-1 and S-2 can be found in Yu and Whittaker (2020).

6.1.1. Hydrodynamic pressure on the wall p_w

Analytical and numerical (ALE and ICFD) results for the time series of p_w at the location of the red solid circle shown in Figure 4 are presented in Figure 11. The red circle is located at (r, θ, z)=(R, 0, 0), which is on the axis of seismic input and at the intersection of the tank wall and base. The pressure at the red solid circle is expected to be the greatest along the fluid depth (Yu and Whittaker, 2020, 2021b). Analytical and numerical results for distributions of p_w are compared along the green line on the tank wall shown in Figure 4: (r, θ, z)=(R, 0, 0 to H). Figure 12 enables the comparison at the time of peak p_w in the time series of Figure 11: see the open green circles. The presented distributions in Figure 12 confirm that the greatest p_w along the fluid depth is on the intersection of the tank wall and base, where the red solid circle is located.

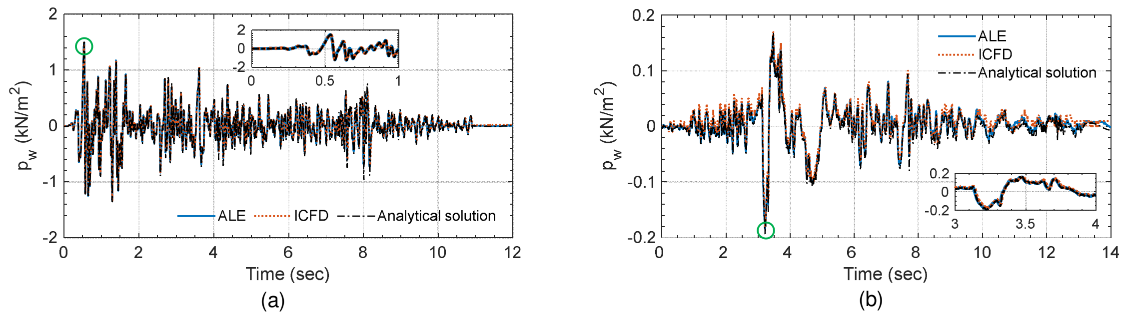

Figure 11. Numerical and analytical results for time series of p_w at the location of the red solid circle shown in Figure 4: (a) E-1; (b) E-2

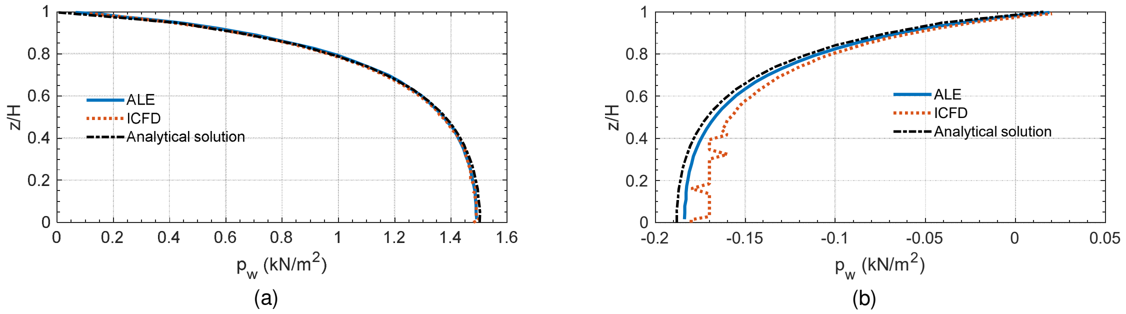

Figure 12. Numerical and analytical results for distributions of p_w along the green line on the tank wall shown in Figure 4, at the time of the peak response noted using open green circles in the corresponding panels of Figure 11: (a) E-1, $t = 0.53$ second; (b) E-2, $t = 3.22$ seconds

6.1.2. Reactions: shear force F and moment M_{wb} at the base

The time series of F in the x direction and M_{wb} about the y axis at the tank base are presented in Figures 13 and 14, respectively. The presented data are calculated using the analytical solutions and numerical models: ALE and ICFD.

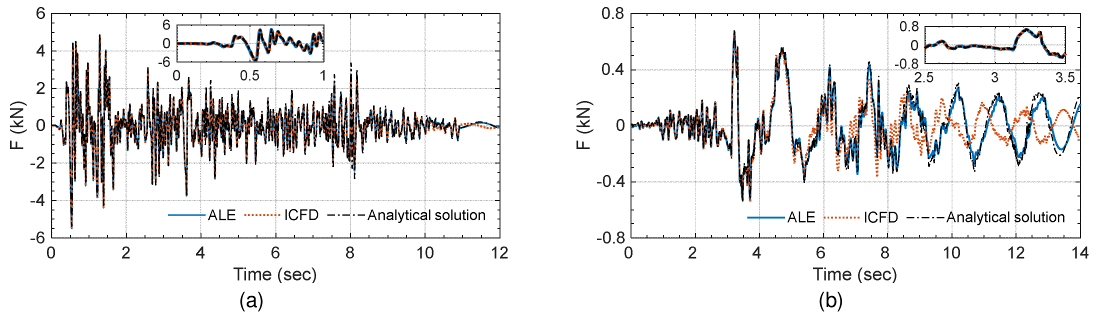

Figure 13. Numerical and analytical results for time series of F in the x direction at the tank base: (a) E-1; (b) E-2

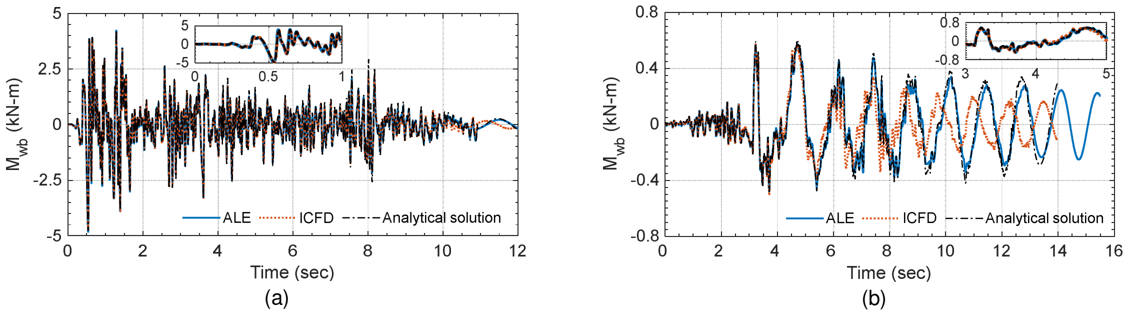

Figure 14. Numerical and analytical results for time series of M_{wb} about the y axis at the tank base: (a) E-1; (b) E-2

6.1.3. Wave height d_w

Analytical and numerical (ALE and ICFD) results for the time series of d_w at the location of the purple triangle shown in Figure 4 are presented in Figure 15. (Information on methods used for tracking the vertical motion of the free surface in the ALE and ICFD models can be found in Yu and Whittaker (2020) and Yu et al. (2021).) The purple triangle is located at (r, θ, z)=(0.7 m, 0, 1.8 m), which is 0.1 R from the tank wall. Although the greatest wave height is expected to be immediately adjacent to the tank wall, the results are reported at the purple triangle because of the boundary effect in the ALE analysis: the vertical fluid velocity on the tank wall is zero, and waves near the wall do not form correctly (more details are presented in Figure 16).

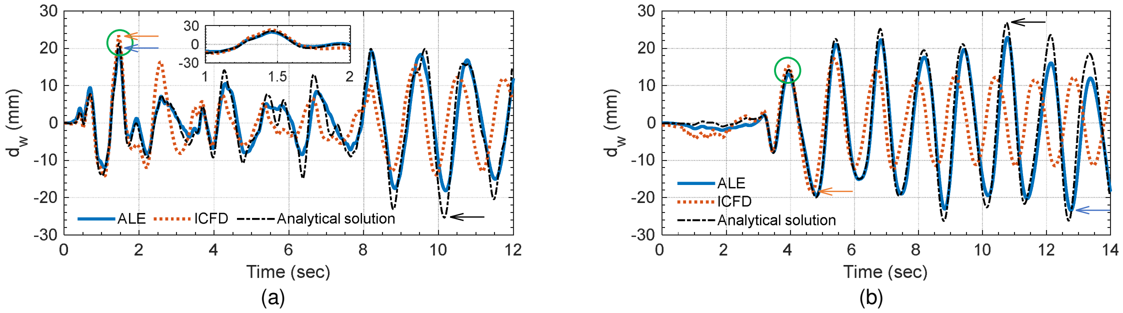

Figure 15. Numerical and analytical results for time series of d_w at the location of the purple triangle shown in Figure 4: (a) E-1; (b) E-2

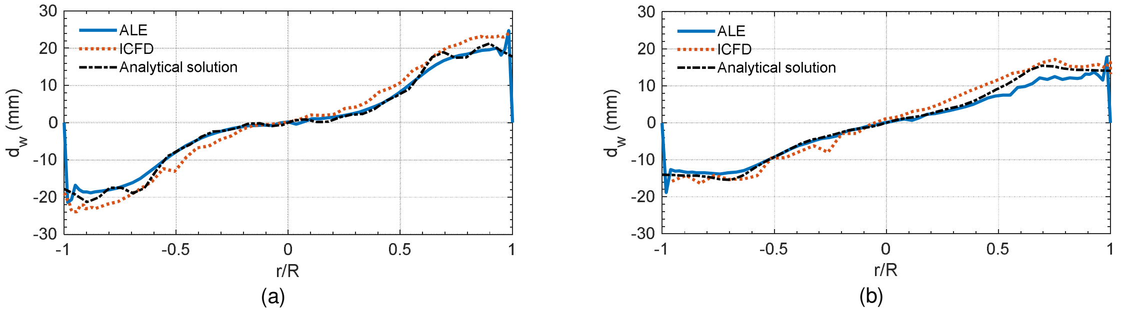

Figure 16. Numerical and analytical results for distributions of d_w along the blue dashed line on the free surface shown in Figure 4, at the time of the peak response noted using open green circles shown in the corresponding panels of Figure 15: (a) E-1 at $t = 1.5$ seconds; (b) E-2 at $t = 3.9$ seconds

Analytical and numerical results for distributions of d_w are compared along the blue dashed line on the free surface shown in Figure 4: (r, θ, z)=($-R$ to R, 0, H). Figure 16 enables the comparison at the time of peak d_w in the time series of Figure 15: see the open green circles. Each open green circle is at a peak in an early stage of a time series, as the ALE, ICFD, and analytical results are in phase. Per Figure 16, the ALE results for the wave height at $r/R = \pm 1$ (adjacent to the wall) are all zero. Wave heights fluctuate near $r/R = \pm 1$ due to the boundary effect in the ALE analysis and stabilize by $r/R \leq \pm 0.9$. The ICFD results presented in Figure 16 do not fluctuate near the tank wall.

6.1.4. Discussion

Table 7 presents the maximum absolute values of p_w, F, M_{wb}, and d_w of the rigid tank subjected to S-1, S-2, E-1, and E-2. The values are extracted from ALE, ICFD, and analytical time series: responses to E-1 and E-2 are presented in Figures 11 and 13 to 15, and those to S-1 and S-2 can be found in Yu and Whittaker (2020). The percentage differences of the ALE and ICFD predictions with respect to the analytical results are presented in parentheses in Table 7. The differences greater than $\pm 10\%$ are bolded. If the differences in a response are less than or equal to $\pm 10\%$ for all four seismic inputs, the ALE or ICFD models are considered to be verified for calculating the response.

As seen in Figures 11 to 14, the ALE (blue lines) and analytical (black dash-dotted lines) results of p_w, F, and M_{wb} for both E-1 and E-2 are in excellent agreement. Per Table 7 the differences between the ALE and analytical results in these responses for all four motions are $\leq \pm 5\%$. Per Figure 15, the ALE time series of d_w are reasonable for the first 5 and 8 seconds of E-1 and E-2, respectively, but thereafter the amplitudes diverge from the analytical results.

Table 7. Maximum absolute fluid-structure responses of a rigid, base-supported, cylindrical tank subjected to unidirectional horizontal motions of a small amplitude, extracted from the ALE, ICFD, and analytical time series

	S-1			S-2		
Responses	Analytical	ALE	ICFD	Analytical	ALE	ICFD
p_w (kN/m^2)	1.5	1.5 (1%)	1.5 (0%)	0.2	0.2 (4%)	0.2 (-1%)
F (kN)	5.5	5.6 (3%)	5.6 (1%)	1.2	1.2 (-1%)	1.1 (-2%)
M_{wb} (kN-m)	4.9	4.9 (1%)	4.9 (1%)	1.3	1.3 (-1%)	1.2 (-3%)
d_w [1] (mm)	8.0	7.7 (-4%)	9.1 **(12%)**	47.3	47.4 (0%)	46.1 (-3%)
	E-1			E-2		
Responses	Analytical	ALE	ICFD	Analytical	ALE	ICFD
p_w (kN/m^2)	1.5	1.5 (-1%)	1.5 (0%)	0.2	0.2 (-2%)	0.2 (-7%)
F (kN)	5.4	5.5 (1%)	5.5 (2%)	0.7	0.7 (1%)	0.7 (-1%)
M_{wb} (kN-m)	4.8	4.8 (0%)	4.8 (1%)	0.6	0.6 (-3%)	0.6 (-2%)
d_w [1] (mm)	24.9	19.6 **(-21%)**	23.5 (-4%)	26.7	23.4 **(-12%)**	18.5 **(-31%)**

1. Maximum absolute responses calculated per the numerical models and analytical solutions occurring at different times

The ALE model underestimates the maximum absolute d_w (peak amplitudes) for both E-1 and E-2 by $\geq \pm 10\%$, as presented in Table 7. The peak amplitudes of the ALE and analytical d_w for each motion presented in Figure 15 occur at different times, noted using blue and black arrows, respectively. Although the ALE model underestimates the amplitudes of d_w, the phases of the time series are in good agreement with the analytical results. The phases are associated with the periods/frequencies of waves (i.e., convective periods/frequencies), which can be identified from the calculated d_w in the frequency domain: Fourier transformation. Figure 17 presents Fourier amplitude spectra for ALE time series of d_w for E-1 and E-2, at 18 locations on the free surface and across the tank diameter in the x direction. The spectral amplitudes are normalized by their maximum ordinates for frequencies ranging between 0 and 3 Hz. The three significant peaks noted using green circles in Figure 17 are associated with the first three convective frequencies calculated using the ALE model: $f_{con,1} = 0.76$ Hz, $f_{con,2} = 1.27$ Hz, and $f_{con,3} = 1.61$ Hz. The first convective frequencies calculated using the analytical solution, for which the equation numbers are listed in Table 4, are 0.76, 1.29, and 1.64 Hz. The differences between the ALE and analytical results are less than 2%.

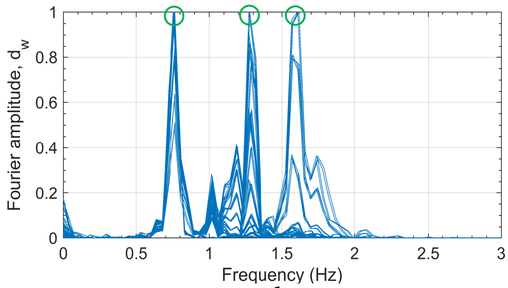

Figure 17. Normalized Fourier amplitude spectra for d_w, at 18 locations along the x direction, $H = 1.8$ m, E-1 and E-2, calculated using the ALE model

On the basis of the comparisons presented above, the ALE model of the rigid base-supported tank is verified for calculating p_w, F, M_{wb}, and $f_{con,j}$, but is limited to analysis of motions with short duration (i.e., 5 to 8 seconds in the analysis here) for calculating d_w.

The differences between the ICFD and analytical results for the amplitudes of p_w, F, and M_{wb} shown in Table 7 are all less than $\pm 10\%$, but those for d_w are greater: 12% for S-1 and -31% for E-2. As presented in Figures 11, 13, and 14, the ICFD and analytical results of p_w, F, and M_{wb} for E-1 are in excellent agreement. However, for E-2, the ICFD (orange dotted lines) and analytical (black dash-dotted lines) results of p_w agree reasonably for $t \le 9$ seconds, and those of F and M_{wb} agree reasonably only for $t \le 5$ seconds. The percentage differences in p_w, F, and M_{wb} for E-2 presented in Table 7 are not affected by the disagreement for $t > 9$ or 5 seconds because their maxima attain at $t = 3.22$ seconds. Per Figure 15, the maxima of the ICFD and analytical d_w for each motion occur at different times, noted using orange and black arrows, respectively. The agreement between the ICFD and analytical time series for d_w is reasonable in the first cycle (a crest and a trough) only: $t \le 1.6$ and 4.5 seconds of E-1 and E-2, respectively. Subsequently, neither the amplitudes nor the phases predicted by the ICFD model are accurate, by comparison with the analytical results: the wave heights and convective periods are both underestimated.

The differences between the ICFD and analytical p_w, F, and M_{wb} for E-2, as presented in Figures 11b, 13b, and 14b, respectively, are linked to inaccurate simulation of the convective component, as seen in the ICFD result for d_w in Figure 15b. As noted in Section 5, E-2 drives waves in the tank due to its great spectral acceleration at $f_{con,1} = 0.76$ Hz, and so the convective component contributes significantly to p_w, F, and M_{wb}. The poor calculation of d_w affects the results of p_w, F, and M_{wb}, and their errors accumulate with time: significant disagreement for $t \ge 9$ or 5 seconds.

According to the comparisons above, the ICFD model of the rigid base-supported tank here is verified for calculating p_w, F, and M_{wb}, if wave action is not significant. The ICFD model is not verified for calculating either wave heights or frequencies.

6.2. FLEXIBLE TANK

Analytical solutions for impulsive responses are used to verify the numerical models of a flexible, base-supported, cylindrical tank ($R = 0.79$ m, $H_s = 2$ m, $H = 2$ m, $h = 0.4$ mm), subjected to S-1 and E-1. (As noted in Sections 2 and 4.2, numerical analysis for the flexible tank sets aside convective responses since analytical solutions for the responses are not available and verification is not possible.) Table 3 presents the equation numbers (Veletsos, 1984; Yu and Whittaker, 2020, 2021b) of the analytical solutions for impulsive frequencies and responses of flexible tanks. The equations per Yu and Whittaker (2021b) are used here. Per Table 3, the impulsive responses are decoupled into modal contributions. The solutions address $f_{imp,k}$, $p_{imp,k}$, $F_{imp,k}$, $M_{imp,w,k}$, and $M_{imp,b,k}$ in the kth impulsive mode.

The first three impulsive frequencies, $f_{imp,1}$, $f_{imp,2}$, and $f_{imp,3}$, of the flexible tank calculated using the numerical models and analytical solution are compared. The frequencies of the tank in the numerical models are identified from the time series of p_{imp} for the sine-sweep motion S-S, at the yellow solid circle shown in Figure 4. The yellow solid circle is located at (r, θ, z)=(R, 0, 0.6H), which is on the axis of seismic input and at a height of 0.6H (with respect to the tank base). The impulsive pressure at the yellow circle is expected to be the greatest along the fluid depth for this flexible tank (Yu and Whittaker, 2020, 2021b) (more information is presented in Section 6.2.1 and Figure 19b). The p_{imp}-time series calculated using the ALE and ICFD models are transformed into the frequency domain and the modal frequencies $f_{imp,1}$, $f_{imp,2}$, and $f_{imp,3}$ are identified from the Fourier amplitude spectra. Figures 18a and b present the spectra calculated using results of the ALE and ICFD models, respectively, normalized by their maximum ordinates. The peaks in the spectra noted using green circles and text are associated with the first three impulsive modes. The impulsive frequencies calculated using the analytical solutions are 24.1, 62.9, and 90.2 Hz for the first three modes. The numerically calculated frequencies noted on the spectra of Figure 18 are different from the analytical results by less than 4%. The third impulsive mode cannot be identified from the ICFD result, but modal responses with a high frequency (i.e., $\geq$90 Hz) can be considered *rigid* and not affected by the calculated frequency.

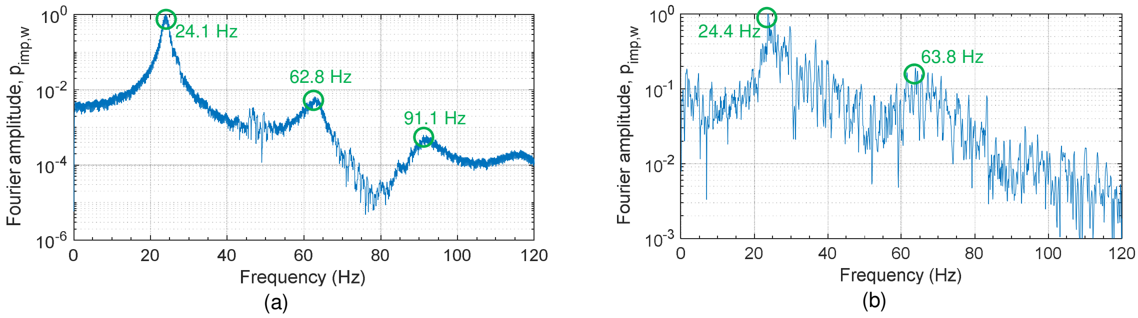

Figure 18. Normalized Fourier amplitude spectra for p_{imp} at the location of the yellow solid circle shown in Figure 4: (a) ALE; (b) ICFD

Response time series of the numerical models and analytical solutions are compared for the impulsive pressure on the tank wall $p_{imp,w}$, shear force F_{imp} at the tank base in the x direction, and moment $M_{imp,wb}$ at the tank base about the y axis. Each impulsive response is the infinite algebraic sum of modal responses (i.e., $k=1$ to ∞), and ten modes are considered here since the contributions of the eleventh and higher modes are negligible. The damping ratio at the frequency of each impulsive mode achieved by the *DAMPING_FREQUENCY_RANGE_DEFORM card (Huang et al., 2019) is used in the analytical calculation. The analytical expression of $p_{imp,w}$ is:

$$p_{imp} = \sum_{k=1}^{10} p_{imp,k} \quad (3)$$

where the equation of $p_{imp,k}$ is taken from Yu and Whittaker (2021b), referenced in Table 3. The moment at the tank base $M_{imp,wb}$ calculated by numerical analysis includes components that balance p_{imp} on the wall and base together: $M_{imp,w}$ and $M_{imp,b}$. Accordingly, the analytical counterpart is calculated as:

$$M_{imp,wb} = M_{imp,w} + M_{imp,b} = \sum_{k=1}^{10} M_{imp,w,k} + \sum_{k=1}^{10} M_{imp,b,k} \tag{4}$$

where the equations of $M_{imp,w,k}$ and $M_{imp,b,k}$ are taken from Yu and Whittaker (2021b) per in Table 3.

Response time series for E-1 are presented in Sections 6.2.1 and 6.2.2, and those for S-1 can be found in Yu and Whittaker (2020).

6.2.1. Impulsive pressure on the wall $p_{imp,w}$

Analytical and numerical (ALE and ICFD) results for the time series of $p_{imp,w}$ at the location of the yellow solid circle shown in Figure 4 are presented in Figure 19a. As seen in Figure 19a, significant response to E-1 is realized in the first second. To reduce run time, the ICFD analysis is performed for 2 seconds only. (The run time of this analysis is about 8 days.) Analytical and numerical results for distributions of $p_{imp,w}$ are compared along the green line on the tank wall shown in Figure 4. Figure 19b enables the comparison at the time of the peak $p_{imp,w}$ noted using an open green circle in Figure 19a. The presented distributions confirm that the greatest $p_{imp,w}$ along the fluid depth is at a height of around $0.6H$, where the yellow circle is located.

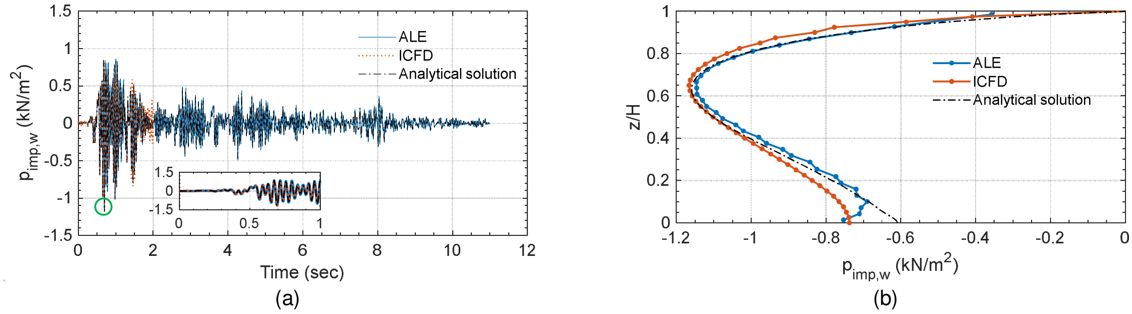

Figure 19. Numerical and analytical results of p_{imp} for E-1: (a) time series at the location of the yellow solid circle shown in Figure 4; (b) distributions along the green line on the tank wall shown in Figure 4 at $t = 0.69$ sec (green circle in the panel a)

6.2.2. Reactions: shear force F_{imp} and moment $M_{imp,wb}$ at the base

The time series of F_{imp} in the x direction and $M_{imp,wb}$ about the y axis at the tank base are presented in Figures 20a and b, respectively. The presented data are calculated using the analytical solutions and numerical models: ALE and ICFD. The ICFD results are calculated for 2 seconds only to reduce the run time.

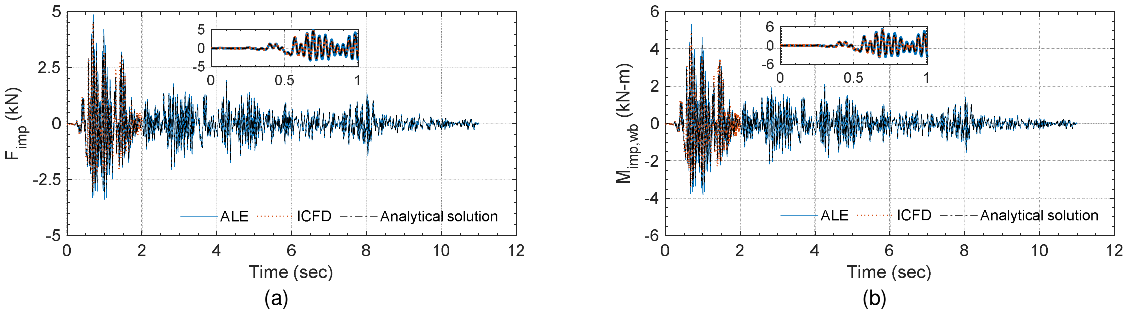

Figure 20. Numerical and analytical results of reaction time series at the tank base for E-1: (a) F_{imp} in the x direction; (b) $M_{imp,wb}$ about the y axis

6.2.3. Discussion

Table 8 presents the maximum absolute values of $p_{imp,w}$, F_{imp}, and $M_{imp,wb}$ for the flexible tank subjected to S-1 and E-1. The values are extracted from the ALE, ICFD, and analytical time series: responses to E-1 are presented in Figures 19a and 20, and those to S-1 can be found in Yu and Whittaker (2020). The percentage differences of the ALE and ICFD predictions with respect to the analytical results are presented in parentheses in Table 8. The differences are $\leq \pm$ 10%. Accordingly, the ALE and ICFD models of the flexible tank are verified for calculating the impulsive responses to unidirectional horizontal motion of a small amplitude.

Table 8. Maximum absolute impulsive responses of a flexible, base-supported, cylindrical tank, subjected to unidirectional horizontal motions of a small amplitude, extracted from the ALE, ICFD, and analytical time series

	S-1			E-1		
Responses	Analytical	ALE	ICFD	Analytical	ALE	ICFD
$p_{imp,w}$ (kN/m^2)	0.6	0.7 (4%)	0.6 (-1%)	1.2	1.1 (-2%)	1.2 (-2%)
F_{imp} (kN)	2.5	2.7 (8%)	2.6 (4%)	4.6	4.9 (7%)	4.5 (-2%)
$M_{imp,wb}$ (kN-m)	2.7	2.9 (10%)	2.8 (6%)	4.9	5.3 (9%)	4.9 (1%)

7. SUMMARY, CONCLUSIONS, AND RECOMMENDATIONS

Earthquake shaking of a liquid-cooled advanced reactor induces fluid-structure interaction (FSI) between the reactor vessel, submerged components, and contained liquid. Verified and validated numerical models for the FSI analysis will be required for the seismic design and qualification of advanced reactors. This paper focuses on the seismic FSI in the reactor vessel and demonstrates a process of verification.

7.1. SUMMARY AND CONCLUSIONS

Numerical models of a base-supported cylindrical tank, with a geometry loosely based on a prototype advanced reactor vessel, are verified. The verification process defined in AIAA (1998) is used: comparison between results calculated using the numerical models and analytical solutions. Seismic FSI analysis of the tank is performed using the ALE and ICFD solvers in LS-DYNA (2018). The analytical solutions used here were originally developed by Jacobsen (1949) and Veletsos (1984), and corrected and re-derived in Yu and Whittaker (2020, 2021b) as needed. To enable the comparison, simplifying assumptions used for the analytical solutions are applied to the models, including 1) rigid or elastic tank, 2) ideal fluid, and 3) small-amplitude, unidirectional, horizontal seismic input. No internal components are included in the analysis. Numerical and analytical results for hydrodynamic pressures on the tank wall, reactions (i.e., shear forces and moments) at the tank base, and wave heights of the contained liquid are compared. According to the reported responses, the ALE model is verified for calculating hydrodynamic pressures, reactions, and convective frequencies for rigid and/or flexible tanks, but is limited to short-duration analysis (e.g., 5 seconds) for calculating wave heights. The ICFD models are not verified for calculating waves (neither heights nor frequencies) but verified for calculating hydrodynamic pressures and reactions for rigid and flexible tanks, if wave action is insignificant or excluded. Accordingly, both solvers require further code development to simulate wave action. If the duration of analysis is short, the ALE solver is the preferred choice of the two solvers studied here.

7.2. RECOMMENDATIONS FOR VERIFICATION PROCESS

The verification process presented here can be broadly applied to seismic FSI analysis of liquid-filled tanks and nuclear equipment. The recommended steps for verification of a numerical model are provided:

1. Identify the application of the numerical model and the required response quantities. For liquid-filled nuclear equipment, hydrodynamic pressures, support reactions, and wave heights are important to seismic analysis and design.
2. Parse the equipment of interest into assemblies based on a hierarchy of complexity in the geometry and liquid (fluid) responses. For example, a nuclear reactor is parsed here into a liquid-filled tank and submerged components. Verify the numerical model of each assembly separately via steps 3 to 8.
3. Develop a conceptual model relevant to the application of the numerical analysis (of an assembly identify in step 2). Accurate solutions (i.e., theoretical, analytical, or differential-equation solutions) for the identified response quantities of the conceptual model must be available.
4. Construct a numerical model for the conceptual model using identical physical properties (e.g., geometry, boundary conditions, initial conditions, and mechanical properties).
5. Perform sensitivity analysis and convergence study to optimize the numerical model. The mesh and time step should be capable of producing responses in the frequency range of interest.
6. Compute numerical results for the response quantities.
7. Compare the numerical results with those calculated using the accurate solutions and quantify the differences.
8. Verify the numerical model per a required threshold (e.g., ± 10%) for the differences between the numerical and accurate results. The threshold is problem- and analyst-specific.
9. Repeat steps 3 to 8 to verify the numerical model of each assembly of the equipment of interest.

The verified models should then be validated. A numerical model of the equipment can then be constructed, informed by the parameters used in the verified (and validated) models, their modeling approach, and limitations for the simulations. Sensitivity analysis and convergence study are required to optimize the numerical model of the equipment.

8. NOTATION

(x, y, z): Cartesian coordinate system, origin at the center of the base of a cylindrical tank

(r, θ, z): cylindrical coordinate system, origin at the center of the base of a cylindrical tank

ρ: density of the fluid in a tank

ρ_s: density of the material of a tank

μ: viscosity of the fluid in a tank

υ_s: Poisson's ratio of the material of a tank

d_w ($d_{w,j}$): vertical displacement of the free surface (in the jth mode) of the fluid in a tank, namely, wave height with respect to the initial free surface

E_s: elastic modulus of the material of a tank

F: shear force at the base of a tank, namely, summation of F_{imp} and F_{con}

F_{con} ($F_{con,j}$): convective shear force (in the jth mode) at the base of a tank

F_{imp} ($F_{imp,k}$): impulsive shear force (in the kth mode) at the base of a tank

$f_{con,j}$: convective frequency of the jth mode of waves in a tank

$f_{imp,k}$: impulsive frequency of the kth mode of a tank

g: gravitational acceleration

H: height of the fluid in a tank with respect to the base

H_s: height of a tank

h: thickness of the wall of a tank

K_w: bulk modulus of the fluid in a tank

$M_{con,b}$ ($M_{con,b,j}$): convective moment (in the jth mode) at the base of a tank generated by $p_{con,b}$

$M_{con,w}$ ($M_{con,w,j}$): convective moment (in the jth mode) at the base of a tank generated by $p_{con,w}$

$M_{imp,b}$ ($M_{imp,b,k}$): impulsive moment (in the kth mode) at the base of a tank generated by $p_{imp,b}$

$M_{imp,w}$ ($M_{imp,w,k}$): impulsive moment (in the kth mode) at the base of a tank generated by $p_{imp,w}$

$M_{imp,wb}$: impulsive moment at the base of a tank, namely, summation of $M_{imp,w}$ and $M_{imp,b}$

M_{wb}: moment at the base of a tank, namely, summation of $M_{imp,w}$, $M_{imp,b}$, $M_{con,w}$, and $M_{con,b}$

p_{con} ($p_{con,j}$): convective pressure (in the jth mode) in the fluid or on the inner surfaces of a tank; p_{con} on the tank wall and base noted as $p_{con,w}$ and $p_{con,b}$, respectively

p_{imp} ($p_{imp,k}$): impulsive pressure (in the kth mode) in the fluid or on the inner surfaces of a tank; p_{imp} on the tank wall and base noted as $p_{imp,w}$ and $p_{imp,b}$, respectively

p_w: hydrodynamic pressure on the wall of a tank, namely, summation of $p_{imp,w}$ and $p_{con,w}$

R: radius of a cylindrical tank

t: time

$u_0''(t)$: acceleration time series of a horizontal ground motion

9. ACKNOWLEDGMENTS

The information, data, or work presented herein was funded in part by the Advanced Research Projects Agency-Energy (ARPA-E), U.S. Department of Energy, under Award Number DE-AR0000978. The views and opinions of the authors expressed herein do not necessarily state or reflect those of the United States Government or any agency thereof.

10. REFERENCES

American Institute of Aeronautics and Astronautics (AIAA) (1998). "Guide for the verification and validation of computational fluid dynamics simulations." *G-077-1998(2002)*, AIAA, Reston, VA.

American Society of Mechanical Engineers (ASME) (2009). "Standard for verification and validation in computational fluid dynamics and heat transfer." *ASME V V 20-2009 (R2016)*, ASME, New York, NY.

American Society of Mechanical Engineers (ASME) (2020). "Standard for verification and validation in computational solid mechanics." *ASME V V 10*, ASME, New York, NY.

ANSYS Inc. (2005). "ANSYS 10.0 user's manual." Cecil Township, PA.

Christovasilis, I. P., and Whittaker, A. S. (2008). "Seismic analysis of conventional and isolated LNG tanks using mechanical analogs." *Earthquake Spectra*, 24(3), 599-616.

Dassault Systèmes (2018). "ABAQUS 2018-unified FEA products." Vélizy-Villacoublay, France.

Fujita, K., Ito, T., Shimomura, T., and Morishita, M. (1984). "Aseismic study on the reactor vessel of a fast breeder reactor." *Nuclear Engineering and Design*, 83(1), 47-61.

Goudarzi, M. A., and Sabbagh-Yazdi, S. R. (2012). "Investigation of nonlinear sloshing effects in seismically excited tanks." *Soil Dynamics and Earthquake Engineering*, 43, 355-365.

Housner, G. W. (1957). "Dynamic pressures on accelerated fluid containers." *Bulletin of the Seismological Society of America*, 47(1), 15-35.

Huang, Y., Sturt, R., and Willford, M. (2019). "A damping model for nonlinear dynamic analysis providing uniform damping over a frequency range." *Computers and Structures*, 212, 101-109.

International Atomic Energy Agency (IAEA) (1999). "Status of liquid metal cooled fast reactor technology." *IAEA-TECDOC-1083*, IAEA, Vienna, Austria.

Jacobsen, L. S. (1949). "Impulsive hydrodynamics of fluid inside a cylindrical tank and of fluid surrounding a cylindrical pier." *Bulletin of the Seismological Society of America*, 39(3), 189-204.

Jensen, S., and Ølgaard, P. (1995). "Description of the prototype fast reactor at Dounreay." *NKS/RAK-2(95)TR-C1*, Rise National Laboratory, Roskilde, Denmark.

Livermore Software Technology Corporation (LSTC) (2018). "LS-DYNA keyword user's manual-R11." LSTC, Livermore, CA.

Ma, D. C., Gvildys, J., and Chang, Y. W. (1983). "Effects of core barrel on vessel seismic loadings." *Tran., 7th International Conference on Structural Mechanics in Reactor Technology (SMiRT-7)*, Chicago, IL.

Mazzoni, S., McKenna, F., Scott, M. H., and Fenves, G. L. (2009). "Open system for earthquake engineering simulation user manual, version 2.0." Pacific Earthquake Engineering Research Center (PEER), University of California, Berkeley, CA.

Mir, F. U. H., Yu, C.-C., and Whittaker, A. S. (2020). "Experimental and numerical studies of seismic fluid-structure interaction in a base-supported cylindrical vessel." *Earthquake Engineering and Structural Dynamics*, 50(5), 1395-1413.

Mir, F. U. H., Yu, C.-C., and Whittaker, A. S. (2021). "Validation of numerical models for seismic analysis of submerged components in advanced reactors." *Proc., 2021 International Topical Meeting on Probabilistic Safety Assessment and Analysis (PSA 2021)*, Columbus, OH.

Oberkampf, W. L., and Trucano, T. G. (2002). "Verification and validation in computational fluid dynamics." *Progress in Aerospace Sciences*, 38(3), 209-272.

Oberkampf, W. L., and Trucano, T. G. (2008). "Verification and validation benchmarks." *Nuclear engineering and Design*, 238(3), 716-743.

Oberkampf, W. L., and Roy, C. J. (2010). *Verification and validation in scientific computing*, 14th Ed., Cambridge University Press, Cambridge, United Kingdom.

Veletsos, A. (1984). "Seismic response and design of liquid storage tanks." Chapter 7 from *Guidelines for the seismic design of oil and gas pipeline systems,* Committee on Gas and Liquid Fuel Lifelines, American Society of Civil Engineers (ASCE), Reston, VA, 255-370.

Yu, C.-C., and Whittaker, A. S. (2020). "Analytical and numerical studies of seismic fluid-structure interaction in liquid-filled vessels." Revision 01 (2021), *MCEER-20-0003*, University at Buffalo, Buffalo, NY.

Yu, C.-C., Mir, F. U. H., and Whittaker, A. S. (2021). "Validation of numerical models for seismic fluid-structure-interaction analysis of nuclear, safety-related equipment." *Nuclear Engineering and Design*, 379, 111179.

Yu, C.-C., and Whittaker, A. S. (2021a). "Verification of numerical models for seismic fluid-structure-interaction analysis of internal components in liquid-filled advanced reactors." *Earthquake Engineering and Structural Dynamics*, 50(6), 1692-1712.

Yu, C.-C., and Whittaker, A. S. (2021b). "Review of analytical studies on seismic fluid-structure interaction of base-supported cylindrical tanks." *Engineering Structures*, 233, 111589.

Zhu, M., McKenna, F., and Scott, M. H. (2018). "OpenSeesPy: Python library for the OpenSees finite element framework." *SoftwareX*, 7, 6-11.